Earth and Planetary Science Letters 541 (2020) 116272

Contents lists available at ScienceDirect

Earth and Planetary Science Letters

www.elsevier.com/locate/epsl

A catalogue of impact craters larger than 200 m and surface age analysis in the Chang'e-5 landing area

Mengna Jia [a,b], Zongyu Yue [a,e], Kaichang Di [a,c,e,*], Bin Liu [a], Jianzhong Liu [d,e], Gregory Michael [f]

[a] State Key Laboratory of Remote Sensing Science, Institute of Remote Sensing and Digital Earth, Chinese Academy of Sciences, Beijing 100101, China
[b] University of Chinese Academy of Sciences, Beijing 100049, China
[c] State Key Laboratory of Lunar and Planetary Sciences, Macau University of Science and Technology, Macau, China
[d] Institute of Geochemistry, Chinese Academy of Sciences, Guiyang 550002, China
[e] CAS Center for Excellence in Comparative Planetology, Hefei 230026, China
[f] Institute of Geological Sciences, Freie Unversitaet Berlin, Malteser Strasse 74-100, Haus D, Berlin 12249, Germany

ARTICLE INFO

Article history:
Received 29 March 2019
Received in revised form 24 February 2020
Accepted 9 April 2020
Available online 23 April 2020
Editor: W.B. McKinnon

Keywords:
craters
Chang'e-5
surface age

ABSTRACT

Chang'e-5 (CE-5) is the first sample-return mission of China's lunar exploration and will be launched in 2020. The planned landing area is near Mons Rümker in Oceanus Procellarum. It is important to have a detailed geological analysis of the landing area prior to the lunar sample collection. The crater size-frequency distribution curve, combined with radioisotope dating of components of the returned sample by CE-5, may allow a refinement of the lunar chronology function. Based on a digital orthophoto map with a pixel size of 1.5 m generated from more than 700 Lunar Reconnaissance Orbiter Camera Narrow Angle Camera images of the CE-5 landing area, all impact craters larger than 200 m in diameter were extracted. Using the resultant crater catalogue of 32,277 craters, a systematic analysis of the landing area including the crater distribution, morphology characteristics, and geologic model ages is conducted. The results show that craters smaller than 1,000 m are denser in the east and the west parts of the region, while those larger than 1,000 m tend to be more concentrated in the central part, particularly within the range of 61.5°W–64.5°W. Within nine geologic units divided using the spectral characteristics, the geologic unit of Em1 (Eratosthenian-aged mare, Em) near the Mons Rümker is the youngest with a model age of $2.02^{+0.16}_{-0.16}$ Ga. The three Rümker plateau (IR) units are the oldest parts of the landing area with the largest model age of $3.49^{+0.073}_{-0.12}$ Ga. The crater catalogue and the surface model age analysis results can contribute to the CE-5 mission as well as further scientific research.

© 2020 Elsevier B.V. All rights reserved.

1. Introduction

The Chang'e-5 (CE-5) mission will be launched as soon as the Long March 5 rocket is prepared. The target area is near Mons Rümker in Oceanus Procellarum, which is a large area of lunar mare on the northwest region of the near-side Moon (Di et al., 2018, 2019). It is China's first sample-return mission and aims to return approximately 2 kg of lunar regolith and rock samples (Yue et al., 2019).

Impact craters are some of the most prominent surface features of terrestrial planets and can provide geologic information and insights into the shallow subsurface structure of planetary bodies (Wilhelms et al., 1978; Head et al., 2010). The crater size-frequency distribution (CSFD) measurement is an important technique used to derive relative and absolute surface model ages (e.g., Shoemaker and Hackman, 1962; Neukum and Ivanov, 1994; Hiesinger et al., 2000, 2003; Michael and Neukum, 2010). Sample-return missions such as the CE-5 mission offer the possibility to provide a refinement of the lunar chronology function (CF) if radioisotope ages obtained from components of the returned samples can be linked to the CSFD of a corresponding surface area. Craters are also potential hazards for landing and therefore, a detailed crater database is important both for scientific research and for engineering safety.

Many global or local lunar crater catalogues have been established using available data. For example, Losiak et al. (2009) integrated previously published data to develop a new lunar crater database including 8,680 craters with diameters ranging from 1 km to 1,000 km. Head et al. (2010) established a global lunar crater catalogue with craters larger than 20 km, including an anal-

* Corresponding author at: No. 20A Datun Road, Chaoyang District, Beijing, 100101, China.
E-mail address: dikc@radi.ac.cn (K. Di).

https://doi.org/10.1016/j.epsl.2020.116272
0012-821X/© 2020 Elsevier B.V. All rights reserved.

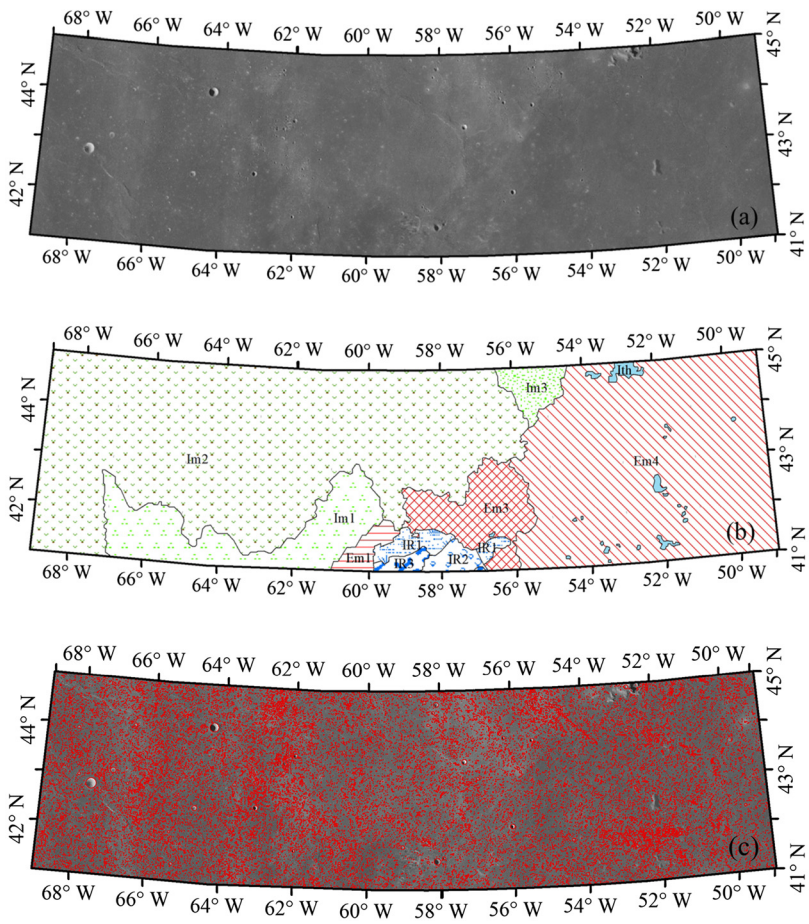

Fig. 1. (a) The basemap of the CE-5 landing area with a pixel size of 1.5 m and generated from LROC NAC images (Di et al., 2018, 2019). (b) The involved geologic units (Qian et al., 2018) of the CE-5 landing area. The small areas exposed within the Em3 and Em4 units are several areas belonging to Ith and Idm units, which were excluded in the surface dating process. (c) The extracted craters (≥200 m) in the CE-5 landing area overlaying on the LROC NAC DOM mosaic. The Lambert conformal conic projection is adopted and north is up.

ysis regarding the crater distribution. Recently, Povilaitis et al. (2018) extended the craters' diameters down to 5–20 km using the basemaps of the Lunar reconnaissance orbiter camera (LROC) Wide Angle Camera (WAC) mosaic (100 m/pixel) (Wagner et al., 2015) and digital terrain model (DTM) (100 m/pixel) (Scholten et al., 2012), which involved 22,746 craters.

More detailed crater catalogues can be established both for the local and global lunar surface using high-resolution images and DTMs, for example from the LROC Narrow Angle Camera (NAC), the Kaguya Terrain Camera (TC), and the Chang'e-2 CCD camera. Based on the data from LROC WAC, LRO Lunar Orbiter Laser Altimeter (LOLA) and Kaguya TC, Robbins (2018) established a global lunar crater database of more than 2 million, within which 1.3 million are larger than 1 km in diameter. For regions related to the CE-5 mission, Qian et al. (2018) used the Kaguya TC global morning image mosaic (Haruyama et al., 2008, 2014) to analyze the crater population in the Rümker region in northern Oceanus Procellarum and determine the absolute model ages of related geologic units. Wu et al. (2018) analyzed the crater and rock distribution in the CE-5 landing area based on LROC NAC images. They detected 48,200 craters that were larger than 100 m.

In this study, we utilize a LROC NAC digital orthophoto map (DOM) mosaic (Di et al., 2018, 2019) and SLDEM2015 (Barker et al., 2016) to obtain a crater catalogue with crater diameters larger than 200 m in the CE-5 landing area. Considering the high spatial resolution and good illumination condition of the images used in generating the DOM mosaic, a reliable CSFD measurement can be expected. Furthermore, the depth of craters is automatically measured from the SLDEM2015. Based on the established crater catalogue, the distribution and morphology characteristics of craters in the CE-5 landing area are analyzed and the model ages for the nine geologic units involved are estimated.

2. Data and method

2.1. LROC NAC images and SLDEM2015

To map craters in the CE-5 landing area, a high-resolution DOM mosaic of the landing area was generated using 765 LROC NAC images and SLDEM2015 (Fig. 1(a)). The SLDEM2015 was generated using a combination of LOLA and stereo-derived DTMs from the Kaguya TC images, which covers latitudes within ±60°. It has a pixel scale of 512 ppd (approximately 60 m at the equator) and a typical vertical accuracy of approximately 3–4 m (Barker et al., 2016). Currently, the LROC NAC obtains the highest resolution lunar orbital images, with the pixel size ranging from 0.5 m to 2.5 m at different flight altitudes (Robinson et al., 2010).

The Experimental Data Record (EDR) level data were first downloaded from the Planetary Data System website (https://ode.rsl.wustl.edu/moon/). The Integrated System for Imagers and Spectrometers (ISIS) software was then used to attach the SPICE kernels (NAIF, 2014) and make radiometric corrections for each image. A block adjustment was then applied to decrease the geometric deviation to the sub-pixel level of NAC images (Di et al., 2018, 2019). The block adjustment simultaneously solves the orientation parameters of the images and the ground coordinates of the tie points

that link the images together, to achieve high accuracy and consistency in a least squares manner. Control points from SLDEM2015 were also incorporated in the block adjustment so that geometric inconsistencies between SLDEM2015 and NAC images could be effectively removed. Finally, a geometrically seamless and radiometrically consistent DOM mosaic was produced with a pixel size of 1.5 m. The DOM mosaic covers an area of 443.7 km × 121.4 km and is centered at (43°N, 59°W). The detailed mapping method can be found in Di et al. (2018, 2019).

2.2. Crater mapping in CE-5 landing area

The craters within the CE-5 landing area were manually digitized from the DOM mosaic with an ArcGIS extension named "CraterTools" (Kneissl et al., 2011). When manually digitizing the craters, the DOM mosaic is shown in a local tangent plane projection with the projection center at (43°N, 59°W) and thus the craters appear circular, making it convenient and precise for crater mapping. Three evenly distributed points on the crater rim were identified to derive the crater diameter with CraterTools, which internally ensured that the crater measurements were not affected by the map projection.

With manual measurements, the crater rim-to-floor depth can be automatically extracted from SLDEM2015 by an ArcGIS add-in developed by Liu et al. (2018). For each crater rim circle, eight evenly distributed profiles crossing the circle center were generated at an angular interval of 22.5°. From each profile, the local maximum of the topographic curvature was determined at the range of ±10% diameter around the manually selected crater rim. If the profile intersecting with other craters, the tool will automatically remove these interfered rim points. End points are manually checked to ensure that they are indeed along the crater rim. Also, manual supplementation may be involved to guarantee that each crater has at least six rim points. Finally, crater depth could be obtained by calculating the average elevation difference between the rim and the floor of each profile. More details of the method can be found in Liu et al. (2018). It is notable that the automatic crater depth extraction process was limited by the resolution and height accuracy of SLDEM2015. Generally, the smallest crater diameter that can be reliably resolved is at least eight pixels across (Garvin and Frawley, 1998; Robbins and Hynek, 2012; Gou et al., 2018). Therefore, only craters larger than 480 m were involved in the automatic depth extraction process.

Secondary craters should be avoided in the surface dating process because they form in large numbers nearly simultaneously, and therefore two surfaces of equal age may differ in crater spatial density by several orders of magnitude (McEwen and Bierhaus, 2006). The proportion (especially at less than 1 km in diameter) and influence of secondary craters on planetary surface have been studied in many papers (e.g., Shoemaker, 1965; Neukum and Ivanov, 1994; Neukum et al., 2001; Hartmann, 2005; Quantin et al., 2007; Bierhaus et al., 2018). Generally, secondary craters occur in chains or clusters around their primary crater with irregular shapes, shallow depths, and herringbone ejecta patterns (e.g., Shoemaker and Hackman, 1962; Oberbeck and Morrison, 1973). However, many authors have pointed out that numerous small circular craters are hardly distinguished as primary or secondary craters from morphology alone (Soderblom et al., 1974; Wilhelms et al., 1978) and the identification of secondaries requires more dedication. In this study, all the craters in chains and clusters with irregular morphologies are mapped as secondary craters and examples can be seen in Fig. S1 of the supplementary file.

There are also several buried craters with shallow profiles and indistinguishable rim borders in this region. An example of the buried crater from NAC DOM mosaic and the SLDEM2015 can be seen in Fig. S2 of the supplementary file. These craters are older than others nearby and are covered by later volcanic lava flows. Therefore, they were also excluded when dating the surface.

2.3. Surface dating with craters

The principle of surface dating from the crater size-frequency distribution is that an aged surface suffers more impact events and accumulates more craters than a young surface. A relative surface model age can thus be determined. With the measured radioisotope ages of returned lunar samples from the Apollo and Luna missions, an absolute model age can be calibrated, consisting of the production function (PF) and the chronology function (Neukum et al., 1975; Neukum, 1983; Neukum and Ivanov, 1994). The PF is established by crater diameter (D) and N_{cum}, which represents cumulative crater density of a geologic unit taken at a fixed reference diameter (usually 1 km and abbreviated as $N(1)$ hereinafter). The deviation of $N(1)$ in each geologic unit can reveal the relative age difference of these units (Neukum, 1983; Neukum and Ivanov, 1994; Hiesinger et al., 2000).

To determine the surface model age with a CSFD measurement, the spatial density of primary craters at every diameter must be calculated (Shoemaker and Hackman, 1962; Boyce, 1976; Neukum and Ivanov, 1994; Hiesinger et al., 2000, 2003). It is important that the mapped craters for dating are within the same geologic unit, that is, accumulated on an area with the same initiation time. A geologic unit can often be understood from spectral and compositional analyses of the surface.

In this study, we adopted the division results of geologic units from Qian et al. (2018), which were determined by the TiO_2 and FeO contents, as well as a false color composite map from the Kaguya Multiband Imager data. There are mainly nine geologic units involved in the CE-5 landing area (Fig. 1(b)), including three Eratosthenian-aged mare (Em1, Em3, Em4) units, three Imbrian-aged mare (Im1, Im2, Im3) units and three Rümker plateau (IR1, IR2, IR3) units. Within the Em3 and Em4 units, there are also several dome units (Idm) and Kipukas/highlands (defined as Ith unit) interpreted to have been formed by the ejecta of the Imbrium basin by Qian et al. (2018).

Moreover, it is worth noting that the regions contaminated by secondaries should be and are excluded from the relevant geologic units when applying CSFD-based dating. The areas of identified secondary craters in this study are illuminated in Fig. S5. With the measured craters in each geologic unit, the absolute model ages can be assessed using the Craterstats2 tool (Michael and Neukum, 2010; http://www.geo.fu-berlin.de/). The Ith and Idm unit-related areas and craters were excluded when dating the Em3 and Em4 units. The lunar PF and CF in the dating process followed Neukum et al. (2001).

A Poisson timing analysis was used to analyze the crater population and obtain the surface model ages with uncertainties because it was independent of the binning width and the application of any type of curve fitting technique (Michael et al., 2016). The derived model age and uncertainties were represented in the percentile format ($m \pm \sigma$), with m being the model age at 50% (median) of the Poisson probability density function and $\pm\sigma$ being ±34% either side of the median.

3. Results

3.1. Catalogue of craters in CE-5 landing area

There were 174,297 craters identified, of which 140,796 and 32,277 craters were larger than 100 m and 200 m, respectively. The mapped results are shown in Fig. 1(c) with the background of the LROC NAC DOM mosaic. There are a number of secondary crater clusters distributed in the research area, which may have

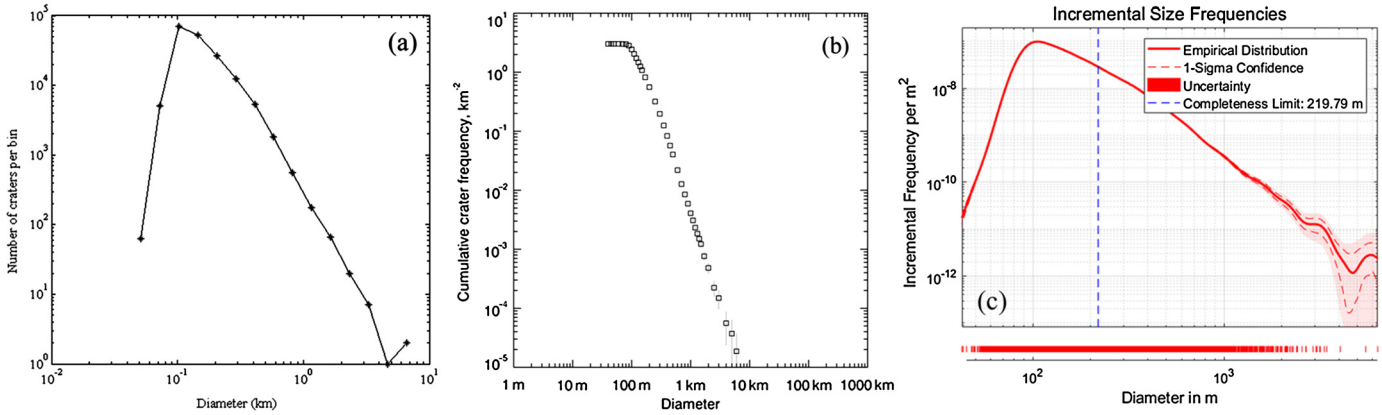

Fig. 2. The (a) incremental and (b) cumulative size-frequency distributions of craters in the established catalogue with the diameter interval set to be $\sqrt{2}D$ in a log-log plot. Note that the diameter axis is the crater median in each bin, which shifts the curves slightly to the larger craters (Robbins et al., 2018). (c) The incremental size-frequency distribution established by robust kernel density estimation (Robbins et al., 2018).

been produced by the craters Copernicus, Harpalus, and Pythagoras (Scott and Eggleton, 1973; Qian et al., 2018). With the easily applicable criteria of irregular shape, clumped distribution and auxiliary information of shallow depth, we manually identified 7,783 and 4,274 secondary craters larger than 100 m and 200 m, respectively, of which 84 were larger than 1 km with the largest diameter being approximately 3 km. These secondary craters and their related areas were excluded from obtaining the model ages. The apparent vertical striping at the left-hand side of Fig. 1(a) (albedo) and Fig. 1(c) (mapped crater density) is due to variable ray density.

The completeness of a crater database describes the minimum size that contains all existing craters (Robbins, 2018), and has been obtained by several different ways in previous researches. For instance, completeness size was determined from the slope change of a cumulative crater size-frequency distribution in Salamunićcar et al. (2012). Robbins and Hynek (2012) adopted the definition that the crater database is complete at one diameter bin larger than that with most craters from an incremental size-frequency distribution (ISFD). In Robbins (2018), the value is estimated by Nth diameter bin larger than where the derivative of the slope is zero in an ISFD.

The size-frequency distributions of craters in our catalogue are depicted in Fig. 2 with incremental and cumulative formats, respectively. The diameters (D) of the craters were binned in $\sqrt{2}D$ intervals. The bin with the largest crater number in Fig. 2(a) has a diameter of ∼100 m, thus the database can be considered complete in ∼150 m with the definition in Robbins and Hynek (2012). By using the method in Salamunićcar et al. (2012), the completeness size can be found to be about 100 m from Fig. 2(b). The zero-slope derivative method by Robbins (2018) indicates that the completeness is ∼200 m (Fig. 2(c)). To be rigorous, the completeness diameter of our crater database is defined as 200 m. Furthermore, Fig. 2 also indicates that the number of craters decreased in a power-law trend with the crater size increasing within the diameter range of 100 m–3.2 km.

The crater spatial density was calculated on a per km^2 basis with the spot size of 1 km × 1 km and a search radius of 5 km for 200 m–1 km craters and 10 km for craters ≥ 1 km. Crater spatial densities for diameters larger than 200 m and 1,000 m are shown in Fig. 3, respectively. There were 233 craters larger than 1,000 m, which was 0.7% of the craters larger than 200 m. The blank areas at the borders of Fig. 3 (c) and (d) were caused by the absence of craters larger than 1,000 m. The low-density areas in Fig. 3 (a) and (b) were generally within Mons Rümker and around large craters, that is, Harding D, Dechen B, and several Rümker craters. There were more craters with D < 1,000 m in the catalogue distributed in the east and the west parts compared with the center area (56°W–60°W). Conversely, craters larger than 1,000 m were predominantly in the central part of the landing area, 61.5°W–64.5°W in particular. Most of the high-density areas within 62°W–64°W, regardless of being smaller sized (200 m–1 km) or larger sized (≥1 km) corresponded to secondary crater clusters or chains (Fig. S1).

The number of craters in each geologic unit was also counted and listed (Table 1). The Im2 unit had the highest crater numbers in all diameter ranges, which was about 45.5% of the total craters larger than 200 m, being the largest of the nine geologic units in the CE-5 landing area. Eight of the top ten largest craters were on Im2 units, including the largest, Harding D crater, which has a diameter of 6.37 km and a depth of 1.27 km and the second largest, Dechen B crater, which has a diameter of 5.52 km and a depth of 1.02 km. The crater spatial density in each geologic unit was calculated by dividing the number of craters by the area (Table 2) in each geologic unit. The Em4 and Im3 units had the highest crater spatial density, both of which are located in the east of the landing area. The results are consistent with those shown in Fig. 3. The Im2 unit had an intermediate crater spatial density, due to the fact that it contained more >1,000 m craters than other geologic units.

The crater depth (d) was estimated with the assistance of SLDEM2015 as described in Section 2.2. Considering the pixel scale of the SLDEM2015, depths were estimated only for craters with diameters larger than 480 m. The SLDEM2015 has a typical vertical accuracy of approximately 3–4 m (Barker et al., 2016) and therefore craters with depths larger than 12 m were used for subsequent analysis. The final number of craters with depth measurements was 2,566, with the depths ranging from 12 m to 1,274 m. Most of the craters (97%) had depths of less than 200 m. Only two craters were deeper than 1 km, with the third-deepest crater being 657 m. Fig. 4 shows the crater depth distribution with a depth interval of 50 m.

The relationship between crater diameter and depth has been widely used to describe the shape of craters such that the depth-diameter (d-D) ratio is considered an important morphologic parameter. The d-D ratios of 2,566 craters were calculated (the histogram is shown in Fig. S4) and primary and secondary craters were analyzed separately. As shown in Fig. 5(a), the diameters and depths for both the primary craters and secondary craters had the positive correlation within the size range of 0.48 km-6 km. The secondary craters had relatively smaller power-law slopes (0.12) compared with those of primary craters (0.19). Fig. 5(b) indicates that primary craters generally had larger d-D ratios than secondary craters. This is consistent with previous research (Pike, 1977; Pike and Wilhelms, 1978).

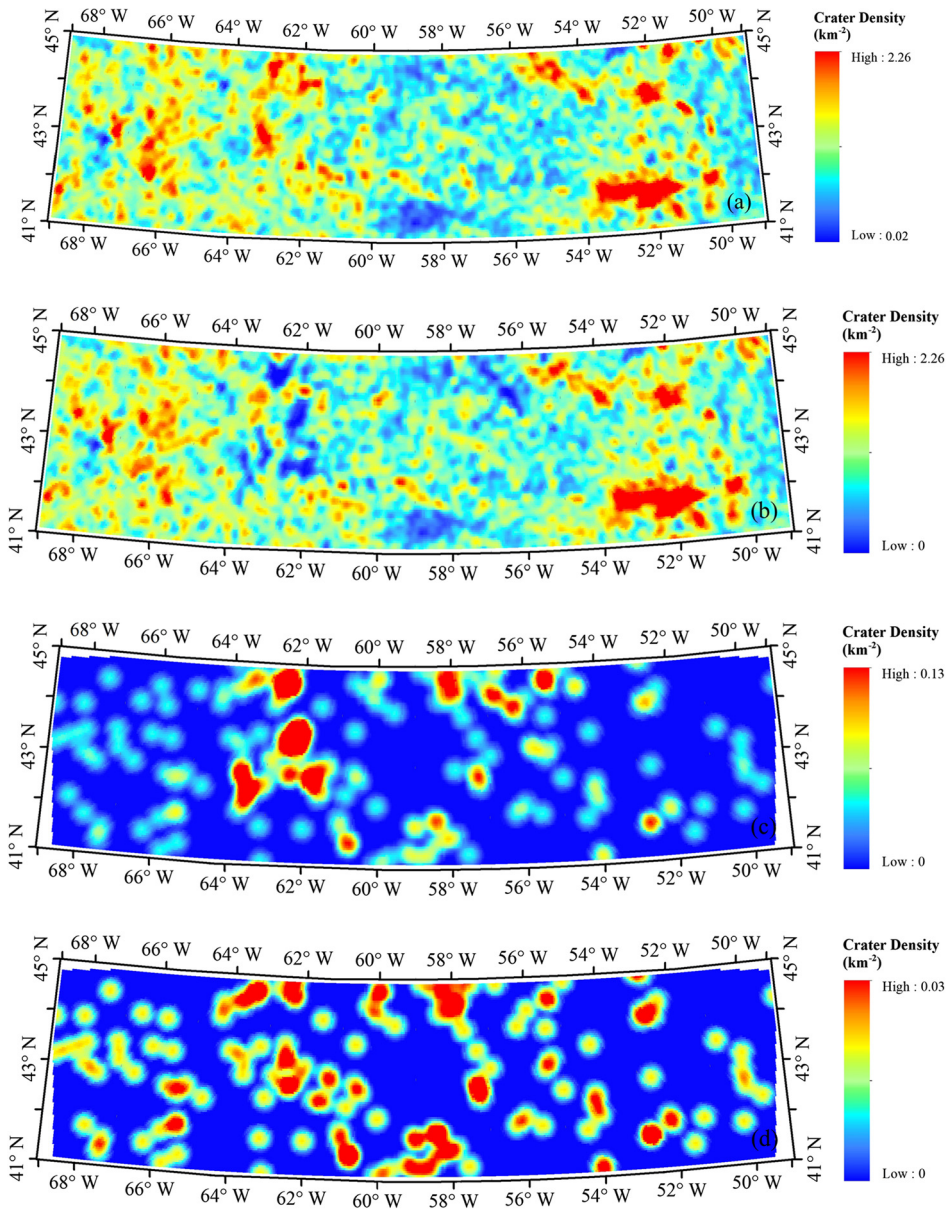

Fig. 3. Crater spatial densities in the CE-5 landing area. (a) crater spatial density including all craters within 200 m–1 km, (b) crater spatial density with D within 200 m–1 km excluding possible secondary craters, (c) crater spatial density including all craters with $D \geq 1$ km, (d) crater spatial density with $D \geq 1$ km excluding possible secondary craters. The Lambert conformal conic projection is adopted and north is up. Note that the colors represent different density values in different plots. (For interpretation of the colors in the figure(s), the reader is referred to the web version of this article.)

Table 1
Number of craters in each geologic unit. The percentiles represent the ratio between the number of craters in each group and the total number of craters (≥200 m) in all nine geologic units. The crater spatial density was calculated by dividing the crater number by the area (Table 2) in each geologic unit.

Geologic Unit	Crater number				Crater spatial density (km^{-2})	
	200 m–1 km	>1 km	Total	Fraction	200 m–1 km	>1 km
Em1	279	1	280	1.0%	0.491	0.002
Em3	1290	9	1299	4.6%	0.457	0.003
Em4	10123	29	10152	36.0%	0.593	0.002
Im1	2570	16	2586	9.2%	0.548	0.003
Im2	12652	155	12807	45.5%	0.490	0.006
Im3	535	9	544	1.9%	0.597	0.010
IR1	164	5	169	0.6%	0.229	0.007
IR2	216	1	217	0.8%	0.462	0.002
IR3	108	2	110	0.4%	0.352	0.007

Table 2
Surface model age dating results of the nine geologic units in this research and results from existing literatures are listed for comparison.

Geologic Unit	Area (km^2)	$N(1)$ ($\times 10^{-3}$ km^2)	Model age (this study; Ga)	Model age (Hiesinger et al., 2003; Ga)	Model age (Qian et al., 2018; Ga)	Model age (Wu et al., 2018; Ga)
Em1	568	1.70	$2.02^{+0.16}_{-0.16}$		$2.30^{+0.10}_{-0.10}$	$2.03^{+0.33}_{-0.33}$
Em3	2823	2.13	$2.54^{+0.41}_{-0.50}$		$1.51^{+0.07}_{-0.07}$	$2.06^{+0.24}_{-0.24}$
Em4	17074	1.74	$2.07^{+0.026}_{-0.027}$	1.33	$1.21^{+0.03}_{-0.03}$	$1.49^{+0.17}_{-0.17}$
Im1	4690	2.99	$3.23^{+0.035}_{-0.042}$	3.47	$3.42^{+0.02}_{-0.02}$	$3.48^{+0.03}_{-0.04}$
Im2	25808	3.10	$3.27^{+0.022}_{-0.025}$	3.44	$3.39^{+0.02}_{-0.02}$	$3.47^{+0.02}_{-0.02}$
Im3	896	3.48	$3.35^{+0.053}_{-0.079}$	3.40	$3.16^{+0.06}_{-0.09}$	
IR1	715	3.96	$3.42^{+0.10}_{-0.21}$		$3.71^{+0.04}_{-0.05}$	$3.57^{+0.04}_{-0.05}$
IR2	468	4.42	$3.47^{+0.061}_{-0.11}$		$3.58^{+0.03}_{-0.04}$	$3.58^{+0.04}_{-0.05}$
IR3	307	4.65	$3.49^{+0.073}_{-0.12}$		$3.51^{+0.04}_{-0.06}$	$3.62^{+0.02}_{-0.02}$

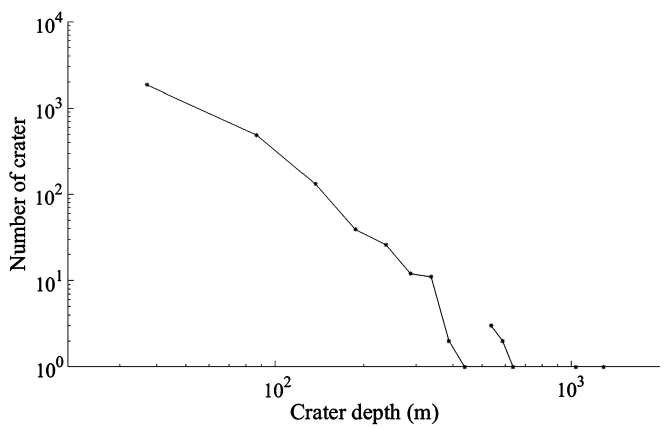

Fig. 4. Crater depth ($D \geq 480$ m) distribution of CE-5 landing area in a log-log plot. There were 2,566 craters catalogued with a depth interval of 50 m. Crater depth in the horizontal coordinate refers to the middle value of each bin, which shifts the curves slightly to the deeper craters (Robbins et al., 2018).

3.2. Surface model ages of CE-5 landing area

The absolute model ages of the nine geologic units were obtained from CSFD measurements with the assistance of the CraterStats2 tool (Michael and Neukum, 2010). The PF and CF were adopted from Neukum et al. (2001). A differential plot was adopted to exhibit the CSFD, which is useful for identifying possible partial resurfacing events (Michael and Neukum, 2010).

A number of secondary craters are present in the research area (see Fig. S1). These secondary craters were excluded in surface dating of the region. The dating results were plotted in Fig. 6 and listed in Table 2. The existence of secondary craters mostly affected the dating results of Em3, Em4 and the three Imbrian-aged mare units.

In Fig. 6, the crater data points used for fitting are marked as black solid squares, and the fitted dating curves are shown as thick black lines. Because larger craters can endure for a longer time and are therefore more likely to hold the best record of the surface formation time, in principle as many as larger craters should be incorporated in surface dating. It can be seen in Fig. 6 that all the large craters are included in fitting the dating curves in this study. All the large craters take effect in the fitting though some of them may not fall exactly on the fitted solid black lines. It is worth noting that some data points in the small end of the crater bin were not used in the curve fitting through selection of fitting range, so that a more accurate fitting can be achieved, i.e., the fitted curve is closer to data points of medium and large sized craters. For comparison purpose, dating curves by using all craters larger than the completeness diameter (200 m) are provided in the supplemental material. It can be observed that including those small craters would make the model age younger; this may be attributed to the effect of resurfacing and/or saturation equilibrium (Michael and Neukum, 2010).

The three Eratosthenian-aged mare units (Em1, Em3 and Em4) were the relatively young units in the research area and Em1 was the youngest unit of the entire region with a model age of $2.02^{+0.16}_{-0.16}$ Ga. The three Rümker plateau units (IR1, IR2 and IR3) were the oldest units and all were older than 3.40 Ga. The three Imbrium-aged mare units had surface model ages occurring between these values. The detailed comparisons of the dating results within the CE-5 landing area with other studies are described in Section 4.2.

4. Discussion

4.1. The analysis of crater depth-diameter ratio in CE-5 landing area

Pike (1977) revealed that typical lunar simple craters (D<15 km) have the depth-diameter ratios of about 0.2. Daubar et al. (2014) used the small craters measured from Apollo-15 landing area and Mare Ingrenii to analyze the *d-D* ratio and the results showed that, within the diameter range of 17.01 m–918.56 m, the average *d-D* ratio is ∼0.1. Sun et al. (2018) investigated *d-D* ratios of fresh craters with diameters smaller than 1 km, resulting the *d-D* ratios ranging from ∼0.1 to ∼0.2.

As shown in Section 3.1, the *d-D* ratios in this study are smaller than the above results, which vary from 0.02 to 0.22. The main reason is that previous researches concerned the *d-D* ratio of fresh craters, which generally have the characteristics of crisp rims, continuous ejecta fresh in appearance, and/or rays around the craters (Pike, 1977; Sun et al., 2018). However, craters in this study contain many degraded craters besides some pristine ones. Fig. 7 shows some craters with low *d-D* ratios; they are heavily degraded with craters B–E identified as secondary craters in this study.

4.2. Dating results compared with previous studies

Several studies have reported the surface model ages of the CE-5 landing area (see Table 2). Hiesinger et al. (2003) performed a CSFD measurement in Oceanus Procellarum and the model ages of four relevant geologic units are listed for comparison. Qian et al. (2018) investigated the Rümker region, which incorporated the research area in this study, and also found absolute model ages of 10 geologic units in the region. However, their research area (39°–46°N, 48°–70°W) was larger than that of this study. The Morning Map data from Kaguya TC images were used to map the

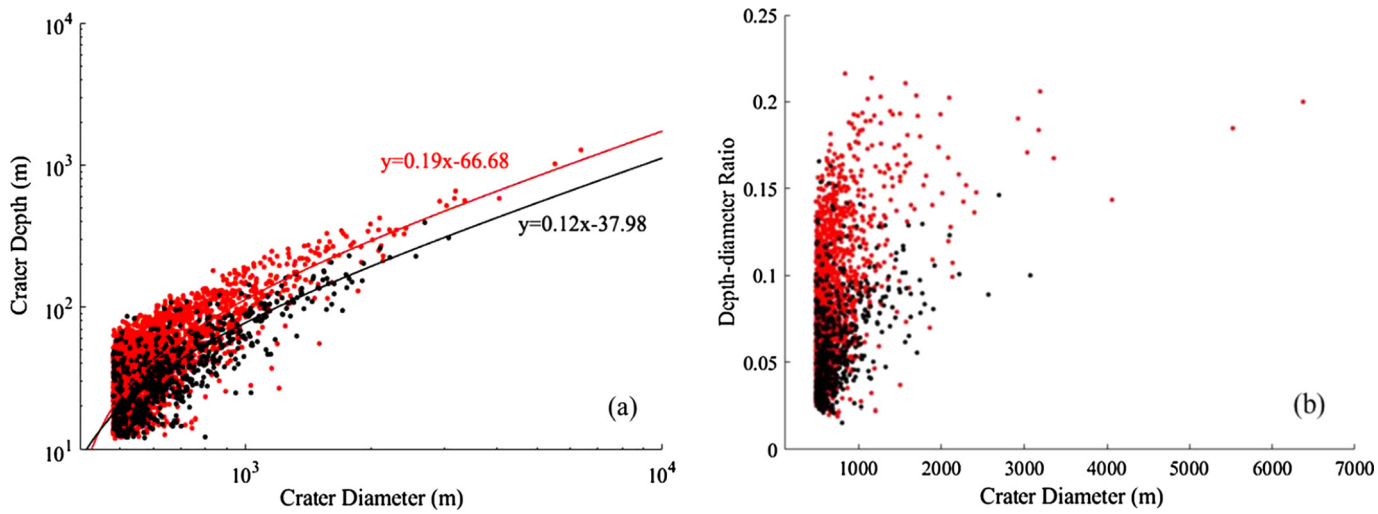

Fig. 5. The relationships between the crater diameter and (a) the crater depth (in a log-log plot), (b) *d-D* ratio, respectively. The results for primary craters are shown in red while the results for identified secondary craters are shown in black. (For interpretation of the colors in the figure(s), the reader is referred to the web version of this article.)

craters in their research, with a pixel size of ∼10 m (Haruyama et al., 2008, 2014) and it is expected that their identification of the smallest craters may not be as precise as that in this research. Furthermore, the limited information about the craters (e.g., the size range and the treatment about secondary craters) used for dating in Qian et al. (2018) makes a detailed comparison to check the reasons for the model age difference difficult.

Wu et al. (2018) performed related work regarding the CE-5 landing area based on the LROC NAC images; however their research area (53°–63°W, 41°–44°N) was smaller than that of this study. An automatic crater detection method (Wang and Wu, 2018) in conjunction with manual checking was used to map craters larger than 100 m and there were 48,200 craters obtained in their research, which is approximately one third of the number of craters obtained here (Section 3.1). This was probably caused by the behavior of the automatic crater identification algorithm: possibly only craters with sharp rims and regular morphology were identified and thus they could only use a fraction of the craters of $D \geq 500$ m for the CSFD analysis. They also adopted similar geologic units to Qian et al. (2018) and their dating results are listed in Table 2.

For the relative model age of different geologic units, we reproduce the results of previous studies indicating that the Eratosthenian-aged mare units are the youngest, followed by the Imbrian-aged mare units, while the Rümker plateau units are the oldest. Nevertheless, smaller differences still exist, with the most likely explanation being the different treatment of the secondary craters. Setting a diameter threshold to exclude the secondary craters, such as in Wu et al. (2018), is a method that is commonly used (e.g., McEwen and Bierhaus, 2006), but may not be the optimal strategy in the CE-5 landing area. As we (Section 3.1 and Fig. 5) and other researchers have found, there are many secondary craters larger than 500 m, and they should also be excluded from dating of the units. Although Wu et al. (2018) implemented manual checking to exclude larger secondary craters, details were not given.

The selection of the crater diameter range representative of the PF is also an important reason for the discrepancies between different studies. In our study, all the measured craters in each geologic unit, after excluding possible secondary craters, are exhibited in Fig. 6; the diameter range has been set for each geologic unit in such a way that all the large bins are included and some small bins are excluded to reach a best fit, i.e., the fitted curve is closer to medium and large sized craters. The comparison in the supplemental material indicates that the dating results reported in this manuscript should be more accurate than that using all craters larger than the completeness diameter. One divergent case between the existing studies and our results can be found in the Em1 unit from Qian et al. (2018) and the Em4 unit from Wu et al. (2018). Their fitted curves do not fit as closely for the larger craters.

The definition of the geologic units also has an effect on the dating results. Although Wu et al. (2018) and our study adopted the geologic units from Qian et al. (2018), there are some differences in the treatment of the enclosed kipuka/highland-related areas in the Em3 and Em4 units. In our study, these areas were excluded, causing an adjustment to the total area, while Wu et al. (2018) included them in the Em3 and Em4 units. Besides, whether one removes areas occupied by secondary craters when calculating a crater spatial density can also lead to the model age disagreement. Other possible reasons for the dating deviations may be factors such as the number of craters involved and differently calculated count areas for the same unit.

4.3. Potential application in future

The establishment of the lunar cratering chronology is based on the combination of radioisotope ages from the lunar returned samples and crater counts of the landing sites (Papanastassiou and Wasserburg, 1971; Neukum, 1983; Neukum and Ivanov, 1994; Hiesinger et al., 2003). CE-5 is a sample-return mission and the radioisotope dating of components from the samples may be able to provide additional absolute age calibrations for the lunar chronology function. Therefore, the crater database and the produced crater size frequency distribution in this research may provide important information to refine the CF.

Besides this, craters are potential hazards for landing. The crater database, as well as the analysis of the crater morphology and distribution, can be a valuable aid for landing site selection to ensure the safety of the mission.

5. Conclusion

This study has established a catalogue for craters larger than 200 m in the CE-5 landing area based on a LROC NAC DOM mosaic with a pixel size of 1.5 m. The crater parameters such as diameter, center latitude and longitude, and depth ($D \geq 480$ m)

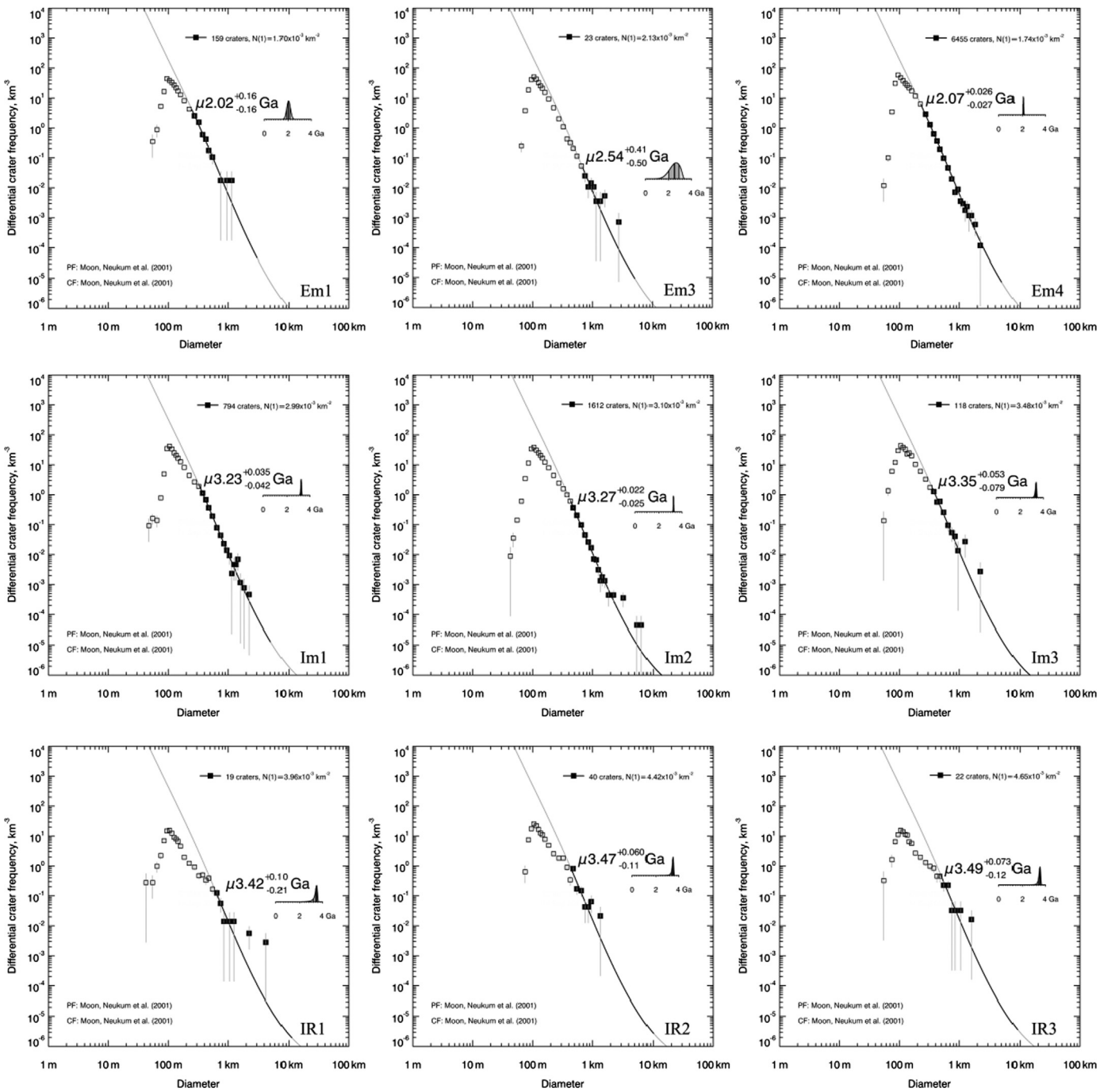

Fig. 6. Dating curves of the nine geologic units excluding possible secondary craters. The crater data points effective for fitting are marked as black solid squares, which are all within the ranges of the fitted dating curves shown as thick black lines. The corresponding isochrons are displayed as gray lines. Data points of small craters not included in fitting are marked as hollow squares.

are included in the database. The crater morphology and distribution in this region is analyzed based on the database. The crater size-frequency distribution was used to obtain the absolute model ages of nine geologic units in the region with higher accuracy than previously. The results indicate that the oldest unit in this region is one of the Rümker plateau units (IR3) with the model age of $3.49^{+0.073}_{-0.12}$ Ga, while the youngest unit is an Eratosthenian-aged mare unit (Em1) with the model age of $2.02^{+0.16}_{-0.16}$ Ga. The established crater database and the obtained model ages are useful for the CE-5 mission and subsequent scientific research.

Declaration of competing interest

The authors declare that they have no known competing financial interests or personal relationships that could have appeared to influence the work reported in this paper.

Acknowledgements

The authors gratefully acknowledge all those who worked on the Planetary Data System archive to make the LROC NAC imagery and SLDEM2015 publicly available. The authors would also like to thank Stuart J. Robbins and William B. McKinnon for great help in

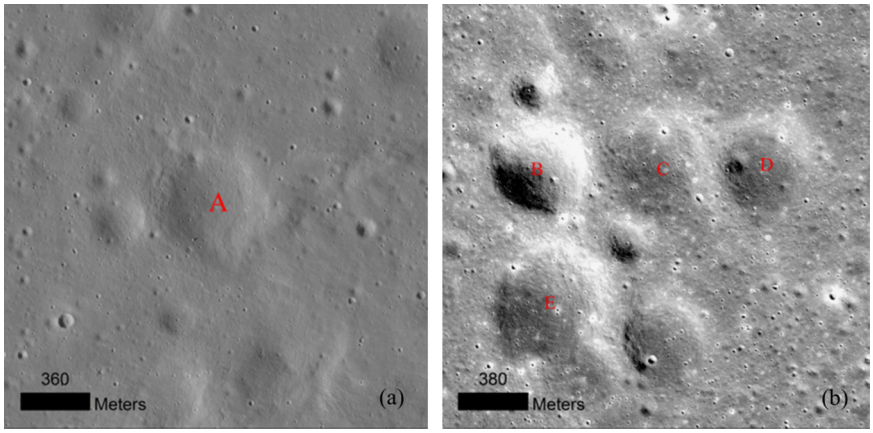

Fig. 7. Examples of small *d*-*D* ratio craters. Crater A has the diameter of 485 m, depth of 19 m and *d*-*D* ratio of 0.04. The three parameters for crater B are 496 m, 46 m, 0.08, for crater C are 584 m, 18 m, 0.03, for crater D are 562 m, 20 m, 0.04, and for crater E are 657 m, 29 m, 0.05. The crater B has a relatively large *d*-*D* ratio compared with the other four labeled craters, which are of similar to the intermediate *d*-*D* ratios of the entire research area. Craters B–E are within a secondary crater chain (Fig. S3) and thus distinguished as secondary craters in this study. North is up.

reviewing this manuscript. This work was supported by the Strategic Priority Program of the Chinese Academy of Sciences (Grant No. XDB41000000), National Natural Science Foundation of China (Grant No. 41490635, 41590851 and 41671458) and Science and Technology Development Fund of Macau (Macau FDCT grant No. 131/2017/A3).

Appendix A. Supplementary material

Supplementary material related to this article can be found online at https://doi.org/10.1016/j.epsl.2020.116272.

References

Barker, M.K., Mazarico, E., Neumann, G.A., et al., 2016. A new lunar digital elevation model from the lunar orbiter laser altimeter and SELENE terrain camera. Icarus 273, 346–355.

Bierhaus, E.B., McEwen, A.S., Robbins, S.J., et al., 2018. Secondary craters and ejecta across the solar system: populations and effects on impact-crater–based chronologies. Meteorit. Planet. Sci. 53 (E8).

Boyce, J.M., 1976. Ages of flow units in the lunar nearside maria based on lunar orbiter IV photographs. In: The 7th Lunar and Planetary Science Conference Proceedings, pp. 2717–2728.

Daubar, I.J., Atwood-Stone, C., Byrne, S., McEwen, A.S., Russell, P.S., 2014. The morphology of small fresh craters on Mars and the Moon. J. Geophys. Res., Planets 119 (12), 2620–2639. https://doi.org/10.1002/2014JE004671.

Di, K., Jia, M., Xin, X., Liu, B., Liu, Z., Peng, M., Yue, Z., 2018. High resolution seamless DOM generation over Chang'e-5 landing area using LROC NAC images. In: 2018 ISPRS TC III Mid-Term Symposium "Developments, Technologies and Applications in Remote Sensing". Beijing, China, 7-10 May, pp. 271–276.

Di, K., Jia, M., Xin, X., Wang, J., Liu, B., Li, J., Xie, J., Liu, Z., Peng, M., et al., 2019. High-resolution large-area digital orthophoto map generation using LROC NAC images. Photogramm. Eng. Remote Sens., 481–491.

Garvin, J.B., Frawley, J.J., 1998. Geometric properties of Martian impact craters: preliminary results from the Mars orbiter laser altimeter. Geophys. Res. Lett. 25 (4), 405–4408.

Gou, S., Yue, Z., Di, K., Liu, Z., 2018. A global catalogue of Ceres impact craters $\geq$ 1 km and preliminary analysis. Icarus 302, 296–307.

Hartmann, W.K., 2005. Martian cratering VIII: Isochron refinement and the chronology of Mars. Icarus 174, 294–320.

Haruyama, J., Matsunaga, T., Ohtake, M., et al., 2008. Global lunar-surface mapping experiment using the lunar imager/spectrometer on SELENE. Earth Planets Space 60, 243–255.

Haruyama, J., Ohtake, M., Matsunaga, T., et al., 2014. Data products of SELENE (Kaguya) terrain camera for future lunar missions. In: 45th Lunar and Planetary Science Conference. Abstract #1304.

Head, J.W., Fassett, C.I., Kadish, S.J., et al., 2010. Global distribution of large lunar craters: implications for resurfacing and impactor populations. Science 329, 1504–1507.

Hiesinger, H., Head, J.W., Wolf, U., Jaumann, R., Neukum, G., 2003. Ages and stratigraphy of mare basalts in oceanus procellarum, mare nubium, mare cognitum, and mare insularum. J. Geophys. Res. 108 (E7), 5056.

Hiesinger, H., Jaumann, R., Neukum, G., Head, J.W., 2000. Ages of mare basalts on the lunar nearside. J. Geophys. Res., Planets 105, 29239–29275.

Kneissl, T., Van Gasselt, S., Neukum, G., 2011. Map–projection–independent crater size-frequency determination in GIS environments–new software tool for ArcGIS. Planet. Space Sci. 59, 1243–1254.

Liu, Z., Yue, Z., Michael, G., Gou, S., Di, K., Sun, S., Liu, J., 2018. A global database and statistical analyses of (4) vesta craters. Icarus 311, 242–257.

Losiak, A., Wilhelms, D.E., Byrne, C.J., et al., 2009. A new lunar impact crater database. In: 40th Lunar and Planetary Science Conference. Abstract #1532.

McEwen, A.S., Bierhaus, E.B., 2006. The importance of secondary cratering to age constraints on planetary surfaces. Annu. Rev. Earth Planet. Sci. 34, 540–567.

Michael, G.G., Kneissl, T., Neesemann, A., 2016. Planetary surface dating from crater size-frequency distribution measurements: Poisson timing analysis. Icarus 277, 279–285.

Michael, G.G., Neukum, G., 2010. Planetary surface dating from crater size–frequency distribution measurements: partial resurfacing events and statistical age uncertainty. Earth Planet. Sci. Lett. 294, 223–229.

NAIF, 2014. Lunar reconnaissance orbiter camera (LROC) instrument kernel v18. http://naif.jpl.nasa.gov/pub/naif/pds/data/lro-l-spice-6-v1.0/lrosp_1000 (last date accessed 10 April 2018).

Neukum, G., 1983. Meteoritenbombardement und Datierung planetarer Oberflächen. Habilitationsschrift (habilitation thesis). Univ. München, Munich, Germany. Meteorite bombardment and dating of planetary surfaces (English translation, 1984). Habilitation Thesis for Faculty Membership, University of Munich, 186 p.

Neukum, G., Ivanov, B.A., 1994. Crater size distributions and impact probabilities on Earth from lunar, terrestrial-planet, and asteroid cratering data. In: Gehrels, T. (Ed.), Hazard Due to Comets and Asteroids. Univ. of Ariz. Press, Tucson, pp. 359–416.

Neukum, G., Ivanov, B.A., Hartmann, W.K., 2001. Cratering records in the inner solar system in relation to the lunar reference system. Space Sci. Rev. 12, 55–86.

Neukum, G., Koenig, B., Arkani-Hamed, J., 1975. A study of lunar impact crater size-distributions. Moon 12 (2), 201–229.

Oberbeck, V.R., Morrison, R.H., 1973. On the formation of the lunar herringbone pattern. In: 4th Lunar Planetary Science Conference, vol. 4, pp. 107–123.

Papanastassiou, D.A., Wasserburg, G.J., 1971. Lunar chronology and evolution from Rb and Sr studies of Apollo 11 and 12 samples. Earth Planet. Sci. Lett. 11 (1), 37–62.

Pike, R.J., 1977. Apparent depth/apparent diameter relation for lunar craters. In: 8th Lunar and Planetary Science Conference, pp. 3427–3436.

Pike, R.J., Wilhelms, D.E., 1978. Secondary-impact craters on the Moon: topographic form and geologic process. In: 9th Lunar and Planetary Science Conference, pp. 907–909.

Povilaitis, R.Z., Robinson, M.S., Van der Bogert, C.H., Hiesinger, H., Meyer, H.M., Ostrach, L.R., 2018. Crater density differences: exploring regional resurfacing, secondary crater populations, and crater saturation equilibrium on the moon. Planet. Space Sci. 162, 41–51.

Qian, Y.Q., Xiao, L., Zhao, S.Y., et al., 2018. Geology and scientific significance of the Rümker region in northern Oceanus Procellarum: China's Chang'E-5 landing region. J. Geophys. Res., Planets 13, 1407–1430.

Quantin, C., Mangold, N., Hartmann, W.K., Allemand, P., 2007. Possible long-term decline in impact rates. 1. Martian geological data. Icarus 186, 1–10.

Robbins, S.J., 2018. A new global database of lunar impact craters> 1–2 km: 1. Crater locations and sizes, comparisons with published databases, and global analysis. J. Geophys. Res., Planets. https://doi.org/10.1029/2018JE005592.

Robbins, S.J., Hynek, B.M., 2012. A new global database of Mars impact craters ≥1 km: 2. Global crater properties and regional variations of the simple-to-complex transition diameter. J. Geophys. Res. 117, E06001.

Robbins, S.J., Riggs, J.D., Weaver, B.P., et al., 2018. Revised recommended methods for analyzing crater size-frequency distributions. Meteorit. Planet. Sci. 53, 891–931.

Robinson, M.S., Brylow, S.M., Tschimmel, M., et al., 2010. Lunar reconnaissance orbiter camera (LROC) instrument overview. Space Sci. Rev. 150, 81–124.

Salamunićcar, G., Lončarić, S., Mazarico, E., 2012. LU60645GT and MA132843GT catalogues of lunar and martian impact craters developed using a crater shape-based interpolation crater detection algorithm for topography data. Planet. Space Sci. 60 (1), 236–247.

Scholten, F., Oberst, J., Matz, K.D., et al., 2012. GLD100: the near-global lunar 100 m raster DTM from LROC WAC stereo image data. J. Geophys. Res., Planets 117 (E12).

Scott, D.H., Eggleton, R.E., 1973. Geologic map of the Rümker quadrangle of the Moon (Map I805). USGS Astrogeology Science Center, Flagstaff.

Shoemaker, E.M., 1965. Preliminary analysis of the fine structure of the lunar surface in Mare Cognitum. Ranger 7, Part 2, Experimenters' Analyses and Interpretations. JPL/NASA Technical Report 32-700, pp. 75–134.

Shoemaker, E.M., Hackman, R.J., 1962. Stratigraphic basis for a lunar time scale. In: Proceedings of the International Astronomical Union, vol. 14, pp. 289–300.

Soderblom, L.A., Condit, C.D., West, R.A., Herman, B.M., Kreidler, T.J., 1974. Martian planetwide crater distributions—implications for geologic history and surface processes. Icarus 22, 239–263.

Sun, S., Yue, Z., Di, K., 2018. Investigation of the depth and diameter relations of subkilometer-diameter lunar craters. Icarus 309, 61–68.

Wagner, R.V., Speyerer, E.J., Robinson, M.S., LROC Team, 2015. New mosaicked data products from the LROC team. In: 46th Lunar and Planetary Science Conference. Abstract #1473.

Wang, Y., Wu, B., 2018. Active machine learning approach for crater detection from planetary imagery and digital elevation models. IEEE Trans. Geosci. Remote Sens.

Wilhelms, D.E., Oberbeck, V.R., Aggarwal, H.R., 1978. Size-frequency distributions of primary and secondary lunar impact craters. In: The 9th Lunar and Planetary Science Conference, pp. 3735–3762.

Wu, B., Huang, J., Li, Y., Wang, Y., Peng, J., 2018. Rock abundance and crater density in the candidate Chang'E-5 landing region on the Moon. J. Geophys. Res., Planets 123, 3256–3272.

Yue, Z., Di, K., Liu, Z., Michael, G., Jia, M., et al., 2019. Lunar regolith thickness deduced from concentric craters in the CE-5 landing area. Icarus 329, 46–54.